



Non-linear interaction of buoyancy with von Kármán's swirling flow in mixed convection above a heated rotating disc



Abhijit Guha, Sayantan Sengupta *

Mechanical Engineering Department, Indian Institute of Technology Kharagpur, Kharagpur 721302, India

ARTICLE INFO

Article history:

Received 5 August 2016

Received in revised form 3 October 2016

Accepted 25 November 2016

Keywords:

Mixed convection

Rotating disc

CFD simulation

Fluid dynamics

ABSTRACT

In this paper, a systematic computational and theoretical study of the thermo-fluid-dynamics governing the flow above a heated horizontal rotating disc is presented. The fluid flow field is much more complex here as compared to von Kármán's original solution (which took into account only the effect of disc rotation), and the effects of non-linear interaction between buoyancy and rotation are critically analysed here by studying the separate and combined roles of disc rotation and buoyancy on the fluid dynamic and heat transfer characteristics. The self-similarity of von Kármán's flow field is lost, and the present paper establishes, for the first time, that the flow field above a heated rotating disc is divided into three distinct fluid dynamic regions. The three regions are demarcated by the loci of $\hat{V}_z = 0$ and $\hat{V}_r = 0$. In region 1 (R-1), \hat{V}_r is positive and \hat{V}_z is negative (such directions of the velocity components are characteristic of von Kármán's flow or pure forced convection). In region 2 (R-2), \hat{V}_r is negative and \hat{V}_z is positive (such directions of the velocity components are characteristic of pure natural convection near a static disc surface). In region 3 (R-3), both \hat{V}_r and \hat{V}_z are negative. The forced convection results are obtained asymptotically at a large non-dimensional radius \mathfrak{R} within the region R-1 showing the dominance of forced convection mechanism, however, the fluid retains the signature of natural convection even at large values of \mathfrak{R} in the region R-3 where there is an inward radial velocity. Similarly, although a plume forms in the central portion of the disc where the solution is dominated by the effects of buoyancy, the fluid retains a signature of the disc rotation in the helical pathlines of fluid particles rising in the plume (whereas there is no swirl velocity present in pure natural convection above a static disc). The non-linear interaction between buoyancy and rotation results in several peculiar, rather non-intuitive, flow phenomena. Examples of such peculiarity include (i) the presence of a very sensitive spot on the upper boundary such that for a small change in this initial position the fluid pathlines may face drastically different final outcomes, (ii) the presence of a small portion near the centre of the disc where the fluid supplies energy to the disc, (iii) the effect of rotation on the rate of convective heat transfer being diminished by buoyancy over certain part of the disc while being enhanced over another part. This non-linear effect on Nusselt number is quantified here in terms of a Grashof number defined for mixed convection (Gr_{mc}).

© 2016 Elsevier Ltd. All rights reserved.

1. Introduction

The study of fluid flow near a rotating disc is important for both its scientific value and engineering application. The famous fluid dynamicist von Kármán provided the first analysis [1] in this field by developing a similarity solution for the flow due to a semi-infinite rotating disc. The similarity solution was established for steady, laminar, incompressible and axi-symmetric flow. Guha and Sengupta [2] has given a lucid physical description of how all three components of the velocity vector, viz. tangential (V_θ),

radial (V_r) and axial (V_z) components, arise in von Kármán's swirling flow. The tangential component is a direct consequence of the disc rotation, whereas the (outward) radial component is an indirect effect. A steady axial flow from the ambient towards the disc occurs to supply the steady radial efflux. An important distinctive feature of a rotational boundary layer is that it, instead of growing continuously like the case of the flat-plate boundary layer, plateaus to a finite thickness which is proportional to $\sqrt{\nu/\Omega}$ where Ω is the angular velocity and ν is the kinematic viscosity of the fluid.

Since the publication of von Kármán's paper, intensive research interest in this field has continued for nearly a century and still new papers are being published. Zandbergen and Dijkstra [3] provided a detailed review on von Kármán's swirling flow. Some

* Corresponding author.

E-mail addresses: a.guha@mech.iitkgp.ernet.in (A. Guha), sayantansengupta@iitkgp.ac.in (S. Sengupta).

recent advances can be found in references [2,4–10]. A description of the contribution of great fluid dynamicists like Ekman [11], Batchelor [12], and Stewartson [13], and, a review of related studies on rotational boundary layer are given in reference [14].

In this paper, the thermo-fluid-dynamics of the flow above a heated horizontal rotating disc is studied. The fluid flow field becomes more complex than von Kármán's swirling flow described above because of the mutual interaction between fluid flow and heat transfer that results into mixed convection. The physical configuration is shown in Fig. 1. r (radial), θ (azimuthal) and z (axial) are the three coordinates and O is the origin of the cylindrical coordinate system. The disc is rotating about the z -axis at an angular speed Ω . The disc-surface is located at $z = 0$ and the solutions given here correspond to $z \geq 0$. The upper surface of the disc is at uniform temperature, which is greater than that of the ambient fluid. The lower surface of the disc is insulated.

Previous papers related to the effect of heat transfer on von Kármán's swirling flow are either theoretical or experimental. A good survey of such work can be found in the review article by Dorfman [15], and also in the monographs written by Kreith [16], Owen and Rogers [17], and Shevchuk [18]. Cobb and Saunders [19] reported an experimental study of heat transfer near a vertically aligned rotating disc, while Elkins and Eaton [20] performed experiments on heat transfer above a heated horizontal rotating disc. Since the experimental set-up and the thermal boundary conditions used in ref [20] correspond to the theoretical study undertaken here, it would be pertinent to give an outline of the experimental procedure here. Elkins and Eaton [20] used a 1 m diameter and 1 mm thick disc. The material of the disc was 304 stainless steel. Below the disc, Kapton thermofoil heaters were attached; and, below the heater, an insulating balsa wood disk 15 mm thick was attached. For structural support a 15 mm thick aluminium disc was attached to the balsa. The measurement of the disc surface temperature could be made throughout the disk using 40 copper-constantan thermocouples. To maintain uniform disc-surface temperature, the disc was split into three different annular regions. The inner disk with a 7.5 cm radius was unheated. The region from 7.5 cm to 20 cm radius was heated by the inner heater and from 20 cm to 48 cm by the outer heater. A control system was used to ensure the uniformity of temperature. It is shown later in the paper (Section 2.6) that the present theoretical prediction of the temperature profile in the forced convection region matches well with the experimental values given by Elkins and Eaton [20]. However, no detailed temperature measurement in the mixed convection region is available in [20].

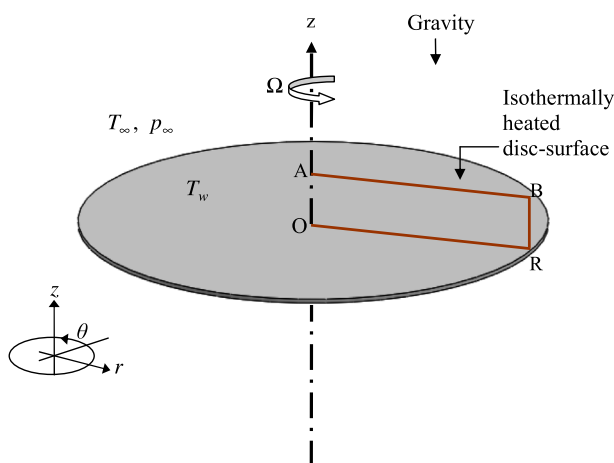


Fig. 1. (Colour online) Schematic diagram of the physical configuration (OABR is a two dimensional computational domain which is used to determine a three-dimensional, axi-symmetric flow field).

Launder and Sharma [21] measured the critical Reynolds number required for the transition from laminar to turbulent flow (details given later). Experimental observations and related discussion on the onset of transition for flow above a rotating disc without heat transfer can be found in Lingwood [22]. For forced convection above a heated rotating disc (i.e. neglecting the effect of natural convection), Wagner [23] derived a theoretical expression for the coefficient of heat transfer considering laminar flow of air. In his paper, Wagner [23] considered approximate profiles for V_r and V_θ within the boundary layer. Theoretical studies on pure natural convection ($\Omega = 0$) above an isothermally heated disc can be found in references [24–26], and interesting discussion on natural convection above a flat, rectangular surface can be found in references [27–30].

A theoretical analysis of mixed convection above a heated rotating disc is presented in a recent paper [31], in which the temperature of the disc-surface (T_w) was assumed to vary quadratically with the radial distance from the disc-centre so that a theoretical solution was possible. Such a temperature boundary condition is restrictive from a practical point of view. We could not find any previous work on mixed convection above a heated rotating disc that is directly relevant for the present study.

1.1. Objective of the present work

The objective of the present paper is to provide a systematic computational fluid dynamic (CFD) study of the laminar mixed convection above an isothermally heated, horizontal rotating disc. As far as we know, a detailed computational study on this topic is not available in the previous literature.

The second objective of this work is to explore and critically expound the detailed fluid dynamic features of mixed convection above a heated rotating disc, and, to express the results in terms of appropriate non-dimensional variables. The fluid dynamics depends on non-linear interaction between buoyancy and rotation, and all the subtleties cannot be quantitatively captured by theoretical (analytical) methods. This establishes the utility of the computational approach.

Finally, the physical understanding is enhanced by studying the separate and combined roles of disc rotation and buoyancy on the fluid dynamic and heat transfer characteristics. A limiting case, in which the effect buoyancy is absent, is devised here by setting $g = 0$ in the CFD simulations. This limiting case represents forced convection for which a similarity theory is also presented. While comparing the results of mixed convection with the results of forced convection, the special effect of buoyancy can be appreciated.

1.2. An early glimpse of the fluid dynamics revealed

The details of the fluid dynamics can be understood only after all the results are presented and explained. However, a brief qualitative overview of the new physics is introduced here in the hope that the conceptual summary given in Fig. 2 will be helpful to interpret the quantitative details presented later. In the original von Kármán's swirling flow, the tendency of a fluid particle from the ambient is to be drawn towards the rotating disc ($V_z \leq 0$) while moving radially outward ($V_r \geq 0$). On the other hand, if the disc is static ($\Omega = 0$) but the disc-surface temperature (T_w) is greater than the temperature of the quiescent fluid (T_∞), then a purely natural convective flow is established. In such flow field, the tangential component of velocity does not exist ($V_\theta = 0$), the radial velocity is inward ($V_r \leq 0$), and the axial velocity (near the disc surface) is away from the disc surface ($V_z \geq 0$) which ultimately results into a central plume. Thus, when buoyancy and rotation are simultaneously present, as above a heated rotating disc – the subject-matter of the present article –, there is a non-linear interaction of

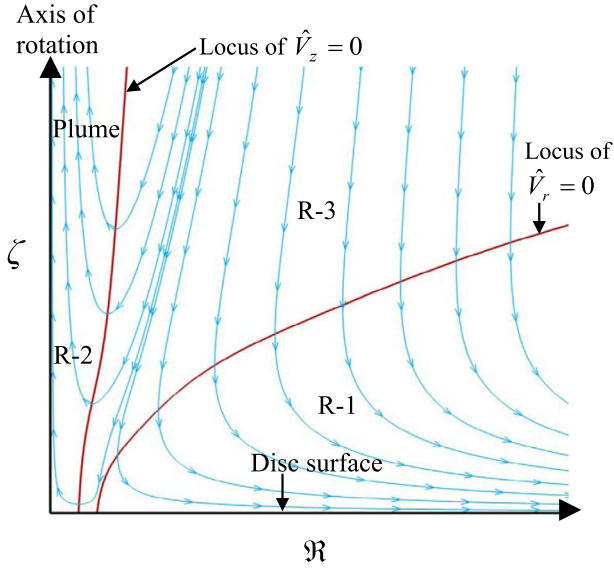


Fig. 2. (Colour online) A schematic, with generic features abstracted from the present CFD simulations, exhibiting three distinct fluid dynamic regions, viz. R-1, R-2 and R-3, above a heated rotating disc. [R-1: a region where \hat{V}_r is positive and \hat{V}_z is negative (located at the bottom of the locus of $\hat{V}_r = 0$), R-2: a region where \hat{V}_r is negative and \hat{V}_z is positive (located at the left of the locus of $\hat{V}_z = 0$), R-3: a region where \hat{V}_r is negative and \hat{V}_z is negative (located between the locus of $\hat{V}_r = 0$ and the locus of $\hat{V}_z = 0$).].

two opposite tendencies of fluid motion. In the central portion of the disc, the effect of buoyancy predominates, whereas at a sufficiently large radius the effect of rotation overtakes the effect of buoyancy. The competition between these two opposing effects results into several interesting flow features. In course of the present investigation it is discovered that the flow field is divided into three separate regions depending on their flow characteristics (as shown in Fig. 2). In region 1 (denoted here as R-1), V_r is positive and V_z is negative (this behaviour of the velocity components is similar to that in von Kármán's swirling flow). In region 2 (R-2), V_r is negative and V_z is positive (as it would be in the case of pure natural convection). There is also a third region (viz. R-3) in which V_r is negative (as it would be in pure natural convection) but V_z is also negative (as it would be in von Kármán's swirling flow or in pure forced convection). As per our knowledge, these flow regimes are identified for the first time in this paper. In most diagrams given later in the results section, two lines representing the loci of $V_z = 0$ and $V_r = 0$, which demarcate the borders between the three regions, are explicitly included so that the nature of the thermo-fluid-dynamic phenomena occurring in the three distinct regions can be appreciated.

2. Solution methodologies

In this section, the governing equations, boundary conditions and the method of CFD simulations for the present mixed convection are given. A set of ordinary differential equations obtained from similarity theory is also provided. The set of ordinary differential equations is obtained by neglecting buoyancy, thus represents forced convection. Under a limiting condition (large non-dimensional radius), the temperature and velocity distributions obtained by the present CFD simulations for mixed convection are validated.

2.1. Governing equations and boundary conditions

Navier-Stokes equations in cylindrical coordinate system are the governing equations for the present problem. Steady, laminar,

axisymmetric, incompressible flow of a Newtonian fluid with constant dynamic viscosity μ , thermal conductivity k and specific heat c_p is considered. Gravity is acting in the negative z -direction (both g_θ and g_r are zero). Viscous dissipation is neglected (according to Gebhart [32], the viscous dissipation term is important only when the induced kinetic energy becomes appreciable compared to the heat transfer). The conservation equations are given below [33].

$$\frac{1}{r} \frac{\partial(rV_r)}{\partial r} + \frac{\partial V_z}{\partial z} = 0 \quad (1)$$

$$\rho \left(V_r \frac{\partial V_r}{\partial r} - \frac{V_\theta^2}{r} + V_z \frac{\partial V_r}{\partial z} \right) = -\frac{\partial p}{\partial r} + \mu \left[\frac{1}{r} \frac{\partial}{\partial r} \left(r \frac{\partial V_r}{\partial r} \right) - \frac{V_r}{r^2} + \frac{\partial^2 V_r}{\partial z^2} \right] \quad (2)$$

$$\rho \left(V_r \frac{\partial V_\theta}{\partial r} + \frac{V_r V_\theta}{r} + V_z \frac{\partial V_\theta}{\partial z} \right) = \mu \left[\frac{1}{r} \frac{\partial}{\partial r} \left(r \frac{\partial V_\theta}{\partial r} \right) - \frac{V_\theta}{r^2} + \frac{\partial^2 V_\theta}{\partial z^2} \right] \quad (3)$$

$$\rho \left(V_r \frac{\partial V_z}{\partial r} + V_z \frac{\partial V_z}{\partial z} \right) = -\frac{\partial p}{\partial z} + f_z + \mu \left[\frac{1}{r} \frac{\partial}{\partial r} \left(r \frac{\partial V_z}{\partial r} \right) + \frac{\partial^2 V_z}{\partial z^2} \right] \quad (4)$$

$$\rho c_p \left(V_r \frac{\partial T}{\partial r} + V_z \frac{\partial T}{\partial z} \right) = \frac{k}{r} \frac{\partial}{\partial r} \left(r \frac{\partial T}{\partial r} \right) + k \frac{\partial^2 T}{\partial z^2} \quad (5)$$

In Eqs. (1)–(5), V_r , V_θ and V_z are respectively the radial, tangential and axial components of absolute velocity. The density ρ is assumed to be constant except in the buoyancy term (Boussinesq approximation). The density ρ in the body force term f_z ($f_z \equiv -\rho g$, where $g = 9.81 \text{ m/s}^2$) is modelled in the following way [34].

$$\rho \approx \rho_\infty - \rho_\infty \beta (T - T_\infty) \quad (6)$$

where, β is the coefficient of thermal expansion. The subscript ∞ represents the ambient condition. For the Boussinesq approximation to be valid, the temperature difference should not be too great.

The boundary conditions for von Kármán's swirling flow above a heated rotating disc are as follows:

$$\text{at } z = 0, V_r = 0, V_\theta = r\Omega, V_z = 0 \text{ and } T = T_w \quad (7)$$

$$\text{as } z \rightarrow \infty, V_r \rightarrow 0, V_\theta \rightarrow 0 \text{ and } T \rightarrow T_\infty \quad (8)$$

2.2. Non-dimensional variables

For all CFD simulations, Prandtl number (Pr), Reynolds number (Re) and Grashof number (Gr) are the inputted non-dimensional numbers. Their expressions are given below.

$$Pr = \frac{\mu c_p}{k}, \quad (9)$$

$$Re \equiv (\Omega r^2)/\nu, \quad (10)$$

and,

$$Gr = \frac{g \beta r^3 (T_w - T_\infty)}{\nu^2}. \quad (11)$$

In Eqs. (10) and (11), ν is the kinematic viscosity of the fluid. The value of Pr depends on fluid properties. For forced convection, CFD solutions depend on Pr and Re . For natural convection, CFD solutions depend on Pr and Gr . For mixed convection, CFD solutions depend on Pr , Re and Gr . For representing the results of mixed convection, a non-dimensional parameter, Gr_{mc} , is introduced. The expression of Gr_{mc} is as follows:

$$Gr_{mc} = \frac{Gr}{Re^{3/2}} = \frac{g\beta(T_w - T_\infty)}{\nu^{1/2}\Omega^{3/2}} \quad (12)$$

For fixed values of Gr_{mc} and Pr , the value of an output non-dimensional variable at any point in a non-dimensional space (under a steady state) is unique. Two useful coordinates of an axi-symmetric non-dimensional space are non-dimensional radius (\mathfrak{R}) and non-dimensional axial coordinate (ζ). The expression of \mathfrak{R} and ζ are given below.

$$\mathfrak{R} = r/\sqrt{\nu/\Omega} = \sqrt{Re}, \quad (13)$$

$$\zeta = z/\sqrt{\nu/\Omega}. \quad (14)$$

The results and the analysis of this paper show that the influence of natural convection diminishes as the radius increases and it is likely that any transition to turbulent flow at large radius will be governed by similar criterion as that of pure forced convection above an unheated rotating disc. Launder and Sharma [21] gives this transition Reynolds number as 10^5 . Eq. (13) shows that, for laminar flow to exist, the non-dimensional radius \mathfrak{R} should not then exceed 316; this criterion is respected in the present computations. Another type of transition to turbulence may take place in the central plume which probably would be governed by the value of local Grashof number (the representative length being the distance above the disc centre). We could not find a definite transition limit in the literature; so we have kept the computational domain such that the maximum Grashof number is well below the transition Grashof number for natural convection on a vertical plate.

The computed variables are also represented in non-dimensional form. The non-dimensional radial velocity \hat{V}_r , the non-dimensional tangential velocity \hat{V}_θ and the non-dimensional axial velocity \hat{V}_z are expressed as follows:

$$\hat{V}_r = V_r/(r\Omega), \quad (15)$$

$$\hat{V}_\theta = V_\theta/(r\Omega), \quad (16)$$

$$\hat{V}_z = V_z/\sqrt{\nu\Omega}. \quad (17)$$

The non-dimensional temperature is denoted by \hat{T} . The expression of \hat{T} is given below.

$$\hat{T} = (T - T_\infty)/(T_w - T_\infty) \quad (18)$$

Non-dimensional moment coefficient ($C_{m,r}$) and Nusselt number (Nu) are two important output parameters of the present CFD simulations. The non-dimensional moment coefficient $C_{m,r}$ represents the non-dimensional torque for a disc segment which is extended from disc-centre up to a radius r . The torque Γ_r required to maintain a steady rotational speed of this disc-segment (against the viscous drag) can be determined by integrating $-2\pi r^2[\tau_{z\theta}]_{z=0}dr$ as given below.

$$\Gamma_r = - \int_0^r 2\pi r^2[\tau_{z\theta}]_{z=0}dr \quad (19)$$

For the present study, torque is computed only on the upper side of the disc. The definition of $C_{m,r}$ [35] is as follows:

$$C_{m,r} = \Gamma_r/(0.5\rho\Omega^2r^5) \quad (20)$$

The definition of Nusselt number is adopted from reference [15]. The local Nusselt number (Nu) is defined as

$$Nu = \frac{q_w r}{k(T_w - T_\infty)}, \quad (21)$$

and, mean Nusselt number (\overline{Nu}) is defined as

$$\overline{Nu} = \frac{\bar{q}_w r}{k(T_w - T_\infty)}. \quad (22)$$

In Eq. (21), q_w is the local surface heat flux. On an isothermal heated disc, q_w varies with radius r . For a disc segment of radius r , the area-averaged surface heat flux \bar{q}_w is expressed as follows:

$$\bar{q}_w = (2/r^2) \int_0^r r q_w dr \quad (23)$$

2.3. CFD method

Navier-Stokes equations are solved by a commercially available CFD (computational fluid dynamics) software Fluent 6.3.26 [36]. Two-dimensional, steady, laminar, double-precision, pressure-based implicit solver, using constant thermophysical properties (viscosity, thermal conductivity and specific heat at constant pressure), is used. The solver uses the time-marching technique [37] to achieve a steady state solution as the limiting process of an unsteady simulation. Axi-symmetric swirl model [36] is used to compute V_θ (the prediction of the axi-symmetric swirl model is verified by comparing it with the result of full three-dimensional simulation, see Appendix A). The SIMPLE algorithm, with second order upwind scheme for momentum and energy equations and second order pressure-discretization, is utilized. Under-relaxation factors for momentum (radial and axial components), swirl (tangential component), energy, pressure, density, and body force are chosen respectively 0.7, 0.9, 1, 0.5, 1 and 1. The convergence criterion for the maximum 'scaled' residual [36] is set as 10^{-7} . When converged, the CFD solution represents that of Eqs. (1)–(5).

Eq. (7), which implies no slip boundary condition on an isothermal disc, can be implemented directly in CFD simulations. A rotational speed (Ω) is specified on the disc-surface. In Fig. 1, OR is the disc-surface located at $z = 0$. Eq. (8) cannot be implemented directly in simulations. The condition $z \rightarrow \infty$ is replaced here by a sufficiently large but finite value of z (which corresponds a large ζ). As per convention [35], a boundary-layer thickness δ is defined to be the axial distance away from the rotating disc at which \hat{V}_θ equals 0.01. For the original von Kármán's flow (with unheated disc-surface), the non-dimensional boundary layer thickness $\hat{\delta}$ ($\hat{\delta} \equiv \delta/\sqrt{\nu_p/\Omega}$) is 5.5 [35]. For the case of heat transfer, other than δ , the thickness of temperature boundary layer needs to be considered. The thickness of temperature boundary layer δ_t is defined as the axial distance away from the rotating disc at which \hat{T} equals 0.01. From similarity solution (Section 2.5), the non-dimensional temperature boundary layer thickness $\hat{\delta}_t$ ($\hat{\delta}_t \equiv \delta_t/\sqrt{\nu_p/\Omega}$) is found to be 8.14. It is expected that, above a heated disc-surface, $\hat{\delta}$ and $\hat{\delta}_t$ are, in general, greater than their respective self-similar values. Therefore, in the present simulations, the ζ -value of the boundary AB (Fig. 1) is set at a location which is much higher than 8.14. At the boundary AB, 'pressure outlet' condition is applied. Present computation demands two additional boundary conditions. The first is an 'axis' boundary condition which is set at OA (Fig. 1). The second is a pressure outlet boundary condition which is set at BR (Fig. 1).

2.4. Grid independence test

A grid independence test has been carried out (Table 1 showing a few pertinent details), and based on this study, a total 81361 (413 × 197) mapped, quadrilateral computational cells are used for the results presented in this paper. The grids are distributed in the radial and axial directions in accordance with the difference in the flow physics in the two directions. The grid distribution in the axial direction is non-uniform with very small grid size close

Table 1
Grid independence test (CFD data given at $Gr_{mc} = 15, Pr = 0.7068$).

Size of the CFD domain	Grid distribution	Number of grids in r and z directions	Total number of computational cells	Nu at $\Re = 10$ from CFD simulations	Nu at $\Re = 75$ from CFD simulations
$[\Re, \zeta] = [0, 0]$ to $[\Re, \zeta] = [215, 60]$	Coarse	(235 × 129)	30315	3.322	24.418
	Standard	(413 × 197)	81361	3.326	24.420
	Fine	(523 × 264)	138072	3.326	24.420

to the disc-surface and with progressively larger grid size towards the boundary AB. Such grid distribution is used to capture the velocity and temperature gradients on the surface ($\zeta = 0$) accurately, and, to resolve the flow physics within the rotational boundary layer. In the present investigation, it is found that both velocity and temperature fields change rapidly at small \Re and slowly at large \Re . In order to capture this effect properly, the grids in the radial direction are divided into two zones – non-uniform and uniform. In the non-uniform zone, very small grids are used close to the disc-centre; and, with an increase in \Re , grid-size is increased progressively. In the uniform zone, the grid size is equal to the size of the last computational cell of the non-uniform zone.

Among several output parameters of the CFD simulations, local Nusselt number (Nu) is selected as a testing parameter for the grid independence test. The values of Nu at two representative non-dimensional radius \Re for various grid distributions are reported in Table 1. For each grid distribution, the implicit (many details about implicit time-marching can be found in [38]) numerical simulation is performed following the method described in Section 2.3. A marginal change of Nu is observed after attaining a grid distribution of 413×197 (see Table 1). A graphical illustration of the success of grid independence achieved close to the axis of rotation, in the region where the gradients of the flow variables are the greatest, has been given in Appendix A. The achieved precision of the numerical solutions lends confidence in the accuracy of the subtle physical characteristics deduced in Section 3.

2.5. Similarity solution

For forced convection, when the effect of buoyancy is absent, it is possible to obtain a set of ordinary differential equations by the application of similarity theory. The set of equations is given below.

$$2\hat{V}_r + \hat{V}_z'' = 0 \tag{24}$$

$$\hat{V}_r^2 - \hat{V}_\theta^2 + \hat{V}_z \hat{V}_r' = \hat{V}_r'' \tag{25}$$

$$2\hat{V}_r \hat{V}_\theta + \hat{V}_z \hat{V}_\theta' = \hat{V}_\theta'' \tag{26}$$

$$\hat{T}'' = Pr \hat{V}_z \hat{T}' \tag{27}$$

In Eqs. (24)–(27), the superscripts single prime and double prime denote $d/d\zeta$ and $d^2/d\zeta^2$, respectively. ζ is defined by Eq. (14). Eqs. (24)–(26) are the same as given by von Kármán [1]. Eq. (27) is an additional equation for obtaining temperature distribution. The necessary boundary conditions are as follows:

$$\text{at } \zeta = 0, \hat{V}_r = 0, \hat{V}_\theta = 1, \hat{V}_z = 0 \text{ and } \hat{T} = 1 \tag{28}$$

$$\text{as } \zeta \rightarrow \infty, \hat{V}_r \rightarrow 0, \hat{V}_\theta \rightarrow 0 \text{ and } \hat{T} \rightarrow 0 \tag{29}$$

Eqs. (24)–(27) are converted into a set of seven first order ordinary differential equations involving $\hat{V}_r, \hat{V}_\theta, \hat{V}_z, \hat{V}_r', \hat{V}_\theta', \hat{V}_z', \hat{T}$ and \hat{T}' ; and, are solved here by the shooting method [39].

It is possible to obtain analytical expressions for $C_{m,r}$ and Nu for the similarity solution. The analytical expression of $C_{m,r}$ [35] is as follows:

$$[C_{m,r}]_{similarity} = -\pi \hat{V}'_\theta(0) / \sqrt{Re} = -\pi \hat{V}'_\theta(0) / \Re. \tag{30}$$

The analytical expression of Nu is as follows:

$$[Nu]_{similarity} = -\sqrt{Re} \hat{T}'(0) = -\Re \hat{T}'(0). \tag{31}$$

In Eq. (30), $\hat{V}'_\theta(0)$ denotes $\partial \hat{V}_\theta / \partial \zeta$ at $\zeta = 0$. Similarly, in Eq. (31), $\hat{T}'(0)$ denotes $\partial \hat{T} / \partial \zeta$ at $\zeta = 0$. From the present numerical solution of Eqs. (24)–(27), the values of $\hat{V}'_\theta(0)$ and $\hat{T}'(0)$ are found to be -0.6159 and -0.325 , respectively.

Present study demonstrates that for fixed values of Gr_{mc} and Pr , the CFD solutions corresponding to mixed convection attain self-similarity for a sufficiently large \Re (see Section 3.2).

2.6. Validation

For fixed values of Gr_{mc} and Pr ($Gr_{mc} = 15, Pr = 0.7068$), Fig. 3 shows the ζ -variations of $\hat{V}_r, \hat{V}_\theta, \hat{V}_z$ and \hat{T} obtained by CFD simulations for mixed convection at $\Re = 75$. For any further increase in \Re , the ζ -profiles of $\hat{V}_r, \hat{V}_\theta, \hat{V}_z$ and \hat{T} vary by a small amount. Fig. 3 shows a good agreement between the CFD solutions at $\Re = 75$ and our own similarity solutions obtained by solving Eqs. (24)–(27). Fig. 3 also contains the numerical solutions of Eqs. (24)–(26), for the variations of $\hat{V}_r, \hat{V}_\theta$ and \hat{V}_z , as given by Owen and Rogers [17]. Fig. 3 further contains the experimental data for

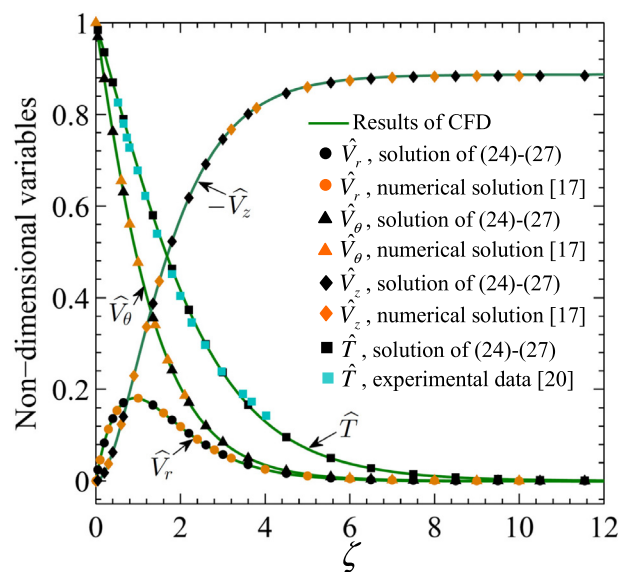


Fig. 3. (Colour online) ζ -distributions of various non-dimensional variables obtained from present CFD simulation, similarity theory and previous literature [Owen and Rogers [17] and Elkins and Eaton [20]]. (CFD simulation is performed at $Gr_{mc} = 15, Pr = 0.7068$. The profiles obtained from CFD are shown for a specific radius, $\Re = 75$; other theoretical values, represented by various symbols, are not dependent on \Re .)

the variation of \hat{T} given by Elkins and Eaton [20]. It can be observed that the present CFD solutions, in the forced convection region, are in good agreement with our own similarity solutions and with other numerical solutions and experimental data available in the literature.

3. Results and discussion

The physical process of mixed convection above a heated rotating disc is explained in this section. The section is divided into four subsections. In Section 3.1, the distributions of \hat{V}_r , \hat{V}_θ , \hat{V}_z and \hat{T} on a \mathfrak{R} - ζ plane are given. In Section 3.2, the ζ -distributions of \hat{V}_r , \hat{V}_θ , \hat{V}_z and \hat{T} at various \mathfrak{R} are given. In Section 3.3, the distributions of local Nusselt number Nu for various mixed convective conditions achieved by varying Gr_{mc} are calculated. Additional computations are performed for calculating the distributions of Nu corresponding to forced convection. The results of mixed convection are compared with the results of forced convection. In Section 3.4, a brief discussion is provided about the trends of integrated output parameters \bar{Nu} and $C_{m,r}$ under various operating conditions.

In order to have a notional feeling regarding the relation (Eq. (13)) between the non-dimensional radius (used in this paper) and the physical size of the disc, we cite a couple of numerical examples. Suppose the fluid is air and the disc is rotating at 700 rpm. Then a non-dimensional radius \mathfrak{R} of 215 would correspond to a disc radius of 10 cm. The same value of \mathfrak{R} (i.e. 215), however, would correspond to a disc radius of 15 cm if the rotational rate is 310 rpm.

3.1. Distributions of velocity and temperature on a \mathfrak{R} - ζ plane

In this section, the distributions of \hat{V}_r , \hat{V}_θ , \hat{V}_z and \hat{T} on a \mathfrak{R} - ζ plane for mixed convection above an isothermally heated rotating disc are provided. Several contour plots are given to describe the details of these distributions. All contours shown in this section are calculated for a representative value of Gr_{mc} (i.e. 15), and for a fixed Pr (i.e. 0.7068).

For the present axisymmetric flow field (which is expressed in the cylindrical polar coordinate system), the relations between the stream function (ψ) and the velocity components are given below:

$$rV_r = -\frac{\partial\psi}{\partial z}, \tag{32}$$

$$rV_z = \frac{\partial\psi}{\partial r}. \tag{33}$$

Eqs. (32) and (33) together satisfy the continuity Eq. (1). Fig. 4a and b display contours of \hat{V}_r and streamlines on a \mathfrak{R} - ζ plane. Fig. 4b provides the details near the axis of rotation.

At the disc surface ($\zeta = 0$), due to no slip boundary condition, \hat{V}_r is zero. In region R-1, fluid flows radially outward ($V_r \geq 0$). Within R-1, with an increase in ζ from the disc surface ($\zeta = 0$), it can be seen that \hat{V}_r first increases, attains a maxima, then decreases and attains a zero value (at the locus of $\hat{V}_r = 0$). With an increase in non-dimensional radius \mathfrak{R} , the \hat{V}_r for mixed convection approaches the self-similar \hat{V}_r . In similarity solution, the maximum \hat{V}_r is 0.1808, whereas, at the start of R-1, \hat{V}_r is substantially small. In R-2, the effect of buoyancy is predominant and a plume is formed. To feed the plume, fluid flows radially inward ($V_r \leq 0$). It is already mentioned in Section 1.2 that \hat{V}_r is negative in both R-2 and R-3. The direction of the fluid flow can also be realised by observing the streamlines. Fig. 4b displays natural convective boundary

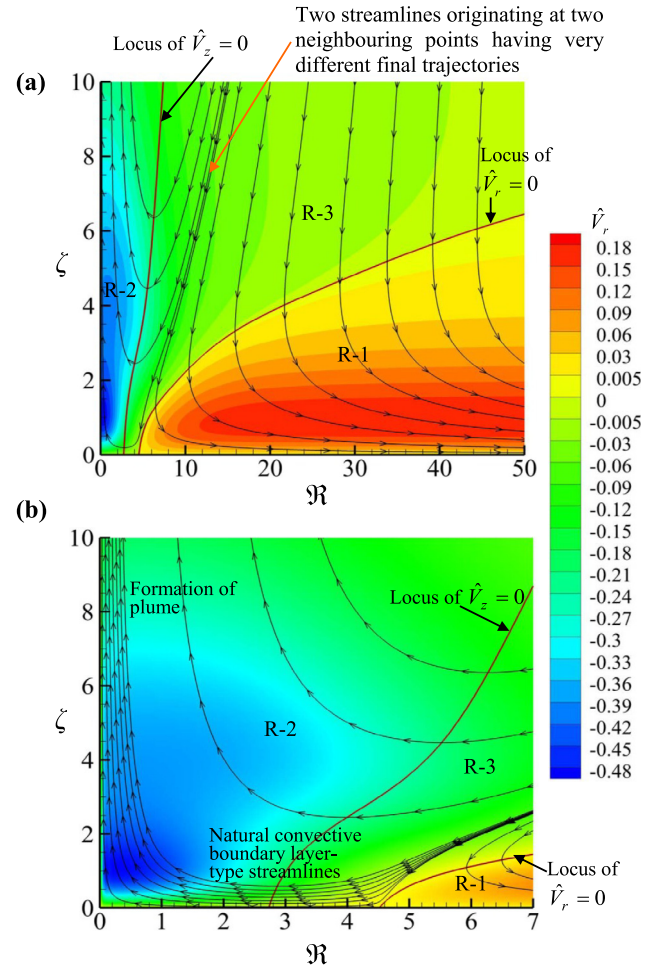


Fig. 4. (Colour online) Contours of non-dimensional radial velocity (\hat{V}_r) and streamlines. (a) Contours of \hat{V}_r for $0 < \mathfrak{R} \leq 50$; (b) Expanded view of the contours of \hat{V}_r close to axis (CFD simulation is performed at $Gr_{mc} = 15$, $Pr = 0.7068$. Streamlines are not drawn according to equispaced streamfunction.).

layer-type streamlines close to disc surface within R-2 and R-3. On the other hand, forced convective boundary layer-type streamlines can be seen within R-1 (Fig. 4a). Fig. 4a shows that there is a sensitive spot on the upper boundary of the computational domain such that two streamlines originating at two neighbouring points may end up in very different final portions of the trajectories, one being drawn into the forced convection domain (moving nearly parallel to the disc surface) while the other is ejected through the plume (moving nearly vertically upward).

Fig. 5 shows contours of \hat{V}_z on a \mathfrak{R} - ζ plane. At the disc surface ($\zeta = 0$), \hat{V}_z is zero due to the no penetration boundary condition. Fig. 5a highlights the regions where \hat{V}_z is negative (i.e. R-1 and R-3). Fluid is entrained through the upper boundary of these regions, and flow within this region is downward. Fig. 5b highlights the region where \hat{V}_z is positive (i.e. R-2). Flow within this region is upward. Such representations are helpful for depicting the details of the variation in \hat{V}_z .

Fig. 5a shows that at a fixed \mathfrak{R} , the magnitude of downward \hat{V}_z within the region R-1 increases with an increase in ζ . The maximum value of downward \hat{V}_z (-0.8845), according to von Kármán's theory, is attained at a large ζ (i.e. mathematically, at $\zeta \rightarrow \infty$). At a sufficiently large \mathfrak{R} , it is expected that the CFD solution within R-1 will almost attain the similarity. This is reflected in Fig. 5a. Fig. 5a shows that when \mathfrak{R} is large the contour lines within R-1 are nearly parallel.

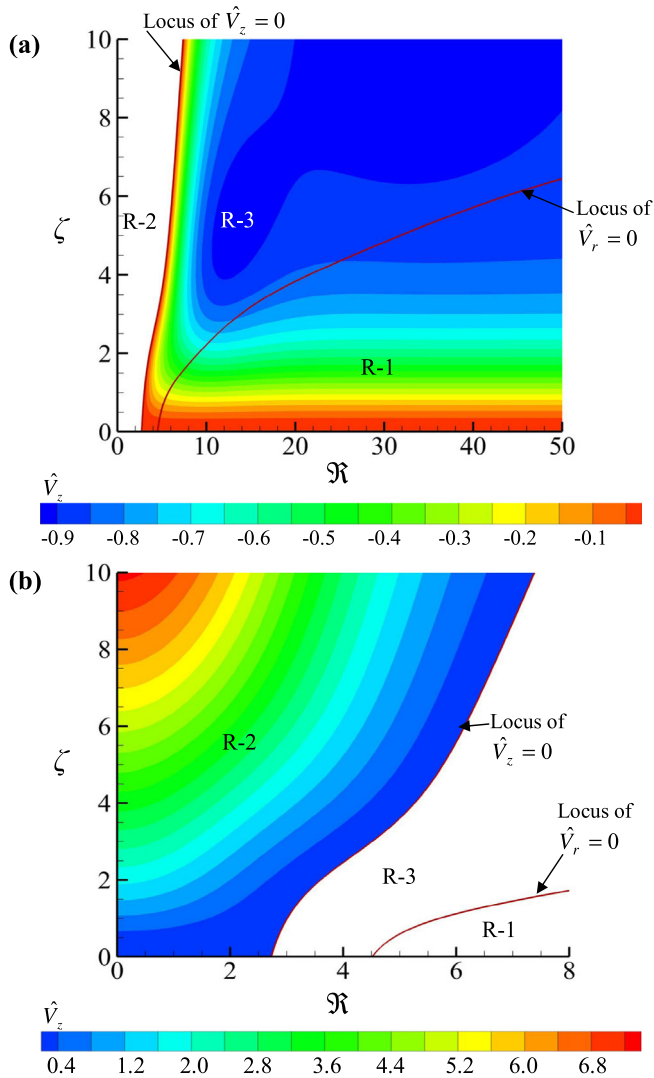


Fig. 5. (Colour online) Contours of non-dimensional axial velocity (\hat{V}_z): (a) the displayed contours correspond to $\hat{V}_z < 0$ (flow is downward); (b) the displayed contours correspond to $\hat{V}_z > 0$ (flow is upward). [CFD simulation is performed at $Gr_{mc} = 15$, $Pr = 0.7068$. Notice the different velocity scales for the two parts (a) and (b). The magnitude of the upward axial velocity in the plume is significantly greater than the downward entrainment velocity at the upper edge of the computational domain.]

Fig. 5b shows that within R-2, where a plume is formed, \hat{V}_z increases with a decrease in \Re . The bending of streamlines within R-2 (Fig. 4) signifies a conversion of radial velocity into axial velocity. The magnitude of the upward axial velocity in the plume is significantly greater than the downward entrainment velocity at the upper edge of the computational domain (Fig. 5a and b). Many features of an axi-symmetric plume developed above a heated static disc are described in reference [26]. A plume developed above a rotating disc has some distinct features which a plume developed over a static disc does not exhibit. These features will be discussed in the context of describing the contours of \hat{V}_θ .

Fig. 6 displays contours of \hat{V}_θ on a \Re - ζ plane. Contour lines, in Fig. 6, are represented by dashed-type discontinuous lines. Due to no-slip boundary condition, \hat{V}_θ is 1 at the disc surface ($\zeta = 0$). The contours for $\hat{V}_\theta \leq 1$ are shown in Fig. 6a; and, the contours for $\hat{V}_\theta \geq 1$ are shown in Fig. 6b. The following observations can be made from Fig. 6a. Within R-1, it can be observed that with an increase in ζ , \hat{V}_θ decreases and approaches to zero. With an

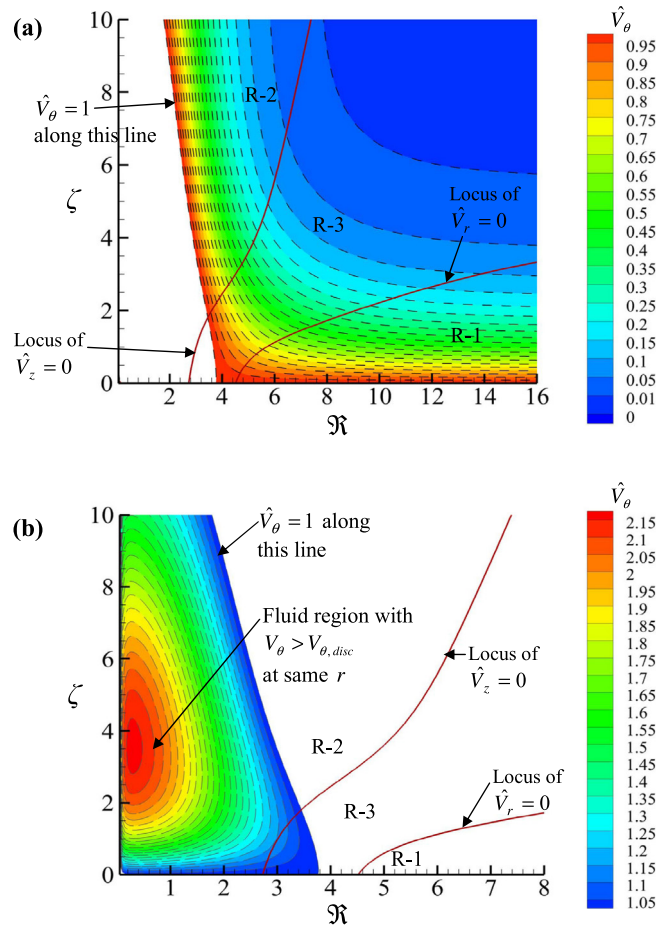


Fig. 6. (Colour online) Contours of non-dimensional tangential velocity (\hat{V}_θ): (a) the displayed contours correspond to $\hat{V}_\theta < 1$; (b) the displayed contours correspond to $\hat{V}_\theta > 1$. [CFD simulation is performed at $Gr_{mc} = 15$, $Pr = 0.7068$. Notice that the maximum value of contour interval displayed in Fig. 6(b) is 2.2, i.e. there are fluid particles which rotate with swirl velocity which is more than 100% greater than the tangential velocity of the disc at the same radius.]

increase in \Re , the contour-lines becomes nearly parallel. This signifies that the CFD solution for \hat{V}_θ approaches to the self-similar solution. (Within R-2 and R-3, the contour-lines are non-parallel.)

Fig. 6b shows that within a portion of regions R-2 and R-3, \hat{V}_θ of the fluid can be significantly greater than unity. This signifies that there are fluid particles which rotate with swirl velocity much greater than the tangential velocity of the disc at the same radius. Fig. 6b shows that the ζ -distribution of \hat{V}_θ is very different from that obtained in von Kármán's swirling flow. With an increase in ζ from the disc surface ($\zeta = 0$), the value of \hat{V}_θ , instead of decreasing, increases, and attains a maxima (>1), and then decreases. The displayed portion in Fig. 6b mainly encapsulates the region where a plume is formed. Unlike a plume developed above a static disc, the \hat{V}_θ component of a plume developed above a rotating disc is non-zero. From Figs. 5b and 6b, it can be inferred that near disc-centre, the hot fluid rises with a swirling motion.

In this context, it is to be mentioned that although Fig. 6b, as compared to Fig. 6a, shows much greater values of \hat{V}_θ , this trend may not hold for the dimensional value of tangential velocity (V_θ). For example, keeping all operating conditions fixed, the dimensional V_θ at $\Re = 10$ is much greater than the dimensional V_θ at $\Re = 1$. This is so because the expression of \hat{V}_θ contains the dimensional r in the denominator (Eq. (16) shows that $\hat{V}_\theta = V_\theta / (r\Omega)$). In von Kármán's solution, the fluid velocity at a fixed

radius decreases with height z . In the present case, fluid entrainment gives rise to complex fluid motion. In those regions, where V_r is negative (inward flow), there is a possibility that the decrease in (dimensional) V_θ due to the action of viscosity for an inwardly advecting fluid particle (coming from a region of greater V_θ due to a greater $V_{\theta,surface}$ at larger radii) is such that its V_θ , although reduced, is still greater than the $V_{\theta,surface}$ at the radial position of its current location. This situation gives rise to the condition $\hat{V}_\theta > 1$. This hypothesis is corroborated by the observation from Fig. 6b that the region with $\hat{V}_\theta > 1$ is a subset of regions of R-2 and R-3 (in both regions V_r is negative).

Fig. 7 shows contours of \hat{T} on a \mathfrak{R} - ζ plane. It can be observed that at any \mathfrak{R} , \hat{T} decreases with an increase in ζ . It is mentioned above that a thermal plume is formed within R-2. Within a plume, the change in temperature is, in general, small. Fig. 7 shows that the magnitude of $\partial\hat{T}/\partial\zeta$ in R-1 is greater than the magnitude of $\partial\hat{T}/\partial\zeta$ in R-2. With an increase in \mathfrak{R} , the contour-lines become nearly parallel. The nearly parallel contour lines indicate that the CFD solution for \hat{T} is close to the self-similar solution. It is also to be noted that at a relatively small value of ζ , similarity is achieved for a relatively small \mathfrak{R} .

3.2. ζ -distributions of velocity and temperature

Fig. 8 shows the ζ -distributions of \hat{V}_r , \hat{V}_θ , \hat{V}_z and \hat{T} at various \mathfrak{R} . All calculations are performed for a representative Gr_{mc} (i.e. 15), and for a fixed Pr (i.e. 0.7068). It can be seen that \hat{V}_r , \hat{V}_θ , \hat{V}_z and \hat{T} nearly attain self-similarity for a sufficiently large \mathfrak{R} . It is to be noted that \hat{V}_θ and \hat{T} approach their respective self-similarity profiles early (see the profiles at $\mathfrak{R} = 9$); and, \hat{V}_r and \hat{V}_z approach their respective self-similarity profiles much later (see the profiles at $\mathfrak{R} = 45$).

The ζ -distributions of \hat{V}_r are shown for four representative values of \mathfrak{R} (i.e. $\mathfrak{R} = 4.5, \mathfrak{R} = 9, \mathfrak{R} = 45$ and $\mathfrak{R} = 75$). At $\mathfrak{R} = 4.5$, \hat{V}_r is negative at all ζ . The flow is radially inward. At $\mathfrak{R} = 9$, \hat{V}_r is positive for small ζ ; and, with a increase in ζ , \hat{V}_r becomes negative. Therefore, at $\mathfrak{R} = 9$, \hat{V}_r is partly positive and partly negative. At $\mathfrak{R} = 45$

and $\mathfrak{R} = 75$, \hat{V}_r is positive up to the locus of $\hat{V}_r = 0$, and a further increase in ζ results into a very small negative value of \hat{V}_r in the region R-3. Therefore, at sufficiently large \mathfrak{R} , the flow is effectively radially outward. At all \mathfrak{R} , the magnitude of \hat{V}_r approaches zero for sufficiently large values of ζ .

The ζ -distributions of \hat{V}_z show that at small \mathfrak{R} , \hat{V}_z is positive (e.g. see the profiles at $\mathfrak{R} = 1, \mathfrak{R} = 2$). This occurs due to the development of a plume near the disc centre. The profile at $\mathfrak{R} = 4.5$ shows both positive and negative values of \hat{V}_z (i.e. \hat{V}_z is negative for small ζ ; and, with a increase in ζ , \hat{V}_z becomes positive). At $\mathfrak{R} = 9$, \hat{V}_z is negative. Therefore, at small values of \mathfrak{R} , the direction of the flow is upward. On the other hand, for the other part of the domain (i.e. at comparatively larger \mathfrak{R}), the direction of the flow is downward. The magnitude of the upward axial velocity is significantly greater than the magnitude of downward axial velocity.

Some distinct characteristics for the variation of \hat{V}_θ are mentioned in Section 3.1. Fig. 8 shows that at small \mathfrak{R} , \hat{V}_θ increases with an increase in ζ . With an increase in \mathfrak{R} (see the profiles at $\mathfrak{R} = 1, \mathfrak{R} = 2$ and $\mathfrak{R} = 3$), the maxima for the profiles of \hat{V}_θ , which are > 1 , shift to a smaller value of ζ . At $\mathfrak{R} = 4.5$, the maxima occurs almost at the disc-surface ($\zeta = 0$); and the value of the maxima is nearly 1. With a further increase \mathfrak{R} , CFD solution approaches to von Kármán's similarity solution (compare the profiles at $\mathfrak{R} = 9$ and $\mathfrak{R} = 45$). It is to be noted that at small \mathfrak{R} , \hat{V}_θ approaches to zero very slowly. Similar trend is observed for the ζ -distributions of \hat{T} . At large \mathfrak{R} (e.g. $\mathfrak{R} = 45$), comparing the ζ -distributions of \hat{T} and \hat{V}_θ , it can be stated that δ_t is greater than δ (typical values of δ_t and δ for the similarity solution are given in Section 2.3).

It is interesting to reveal how, with increasing \mathfrak{R} , the CFD solution for mixed convection progressively approaches towards the self-similar solution of forced convection. With this objective, for a representative Gr_{mc} (i.e. 15) and for a fixed Pr (i.e. 0.7068), the axial variation of \hat{V}_r for various values of \mathfrak{R} are calculated from CFD simulations. Fig. 9 shows these calculated \hat{V}_r -profiles. The same figure also shows the unique \hat{V}_r -profile obtained from the similarity theory for forced convection. ζ is plotted as the ordinate so that the vertical sense is retained for easy physical interpretation. The lowest \mathfrak{R} shown in this diagram (i.e. $\mathfrak{R} = 4.5$) indicates the \mathfrak{R} -location where the region R-1 just starts for the selected Gr_{mc} and Pr . With an increase in \mathfrak{R} , the progressive development of the \hat{V}_r -profiles for mixed convection towards the unique self-similar \hat{V}_r -profile can be observed in Fig. 9. Within R-1, the \hat{V}_r -profile corresponding to a particular \mathfrak{R} has a maxima. The maximum value of \hat{V}_r is denoted as $\hat{V}_{r,max}$, and the value of ζ corresponding to a $\hat{V}_{r,max}$ is denoted as $\zeta_{\hat{V}_{r,max}}$. Fig. 9 shows that with an increase in \mathfrak{R} , both $\hat{V}_{r,max}$ and $\zeta_{\hat{V}_{r,max}}$ for mixed convection approach to their respective self-similar values (from similarity solution, $\hat{V}_{r,max} = 0.1808$ and $\zeta_{\hat{V}_{r,max}} = 0.93$). However, Fig. 9 also shows that even for $\mathfrak{R} = 45$, the asymptotic values of \hat{V}_r at large ζ show qualitatively different behaviour: the \hat{V}_r in self-similar profile asymptotically approaches zero from the positive side, but \hat{V}_r in mixed convection assumes a finite negative value (corresponding to Region R-3).

3.3. Distribution of local Nusselt number (Nu)

Local Nusselt number Nu is defined in Section 2.2 (see Eq. (21)). For a fixed Pr , CFD simulations are carried out for various Gr_{mc} . Fig. 10a shows the variations of Nu with non-dimensional radius \mathfrak{R} for three representative values of Gr_{mc} . The figure also contains

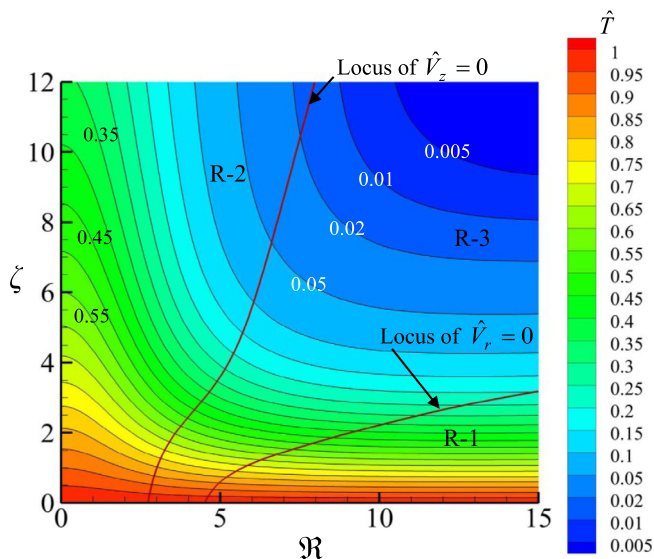


Fig. 7. (Colour online) Contours of non-dimensional temperature (\hat{T}) above an isothermally-heated, rotating disc-surface. [CFD simulation is performed at $Gr_{mc} = 15$, $Pr = 0.7068$. Note that the contour-lines are nearly parallel at large non-dimensional radius \mathfrak{R} but the slopes change drastically with a decrease in \mathfrak{R} .]

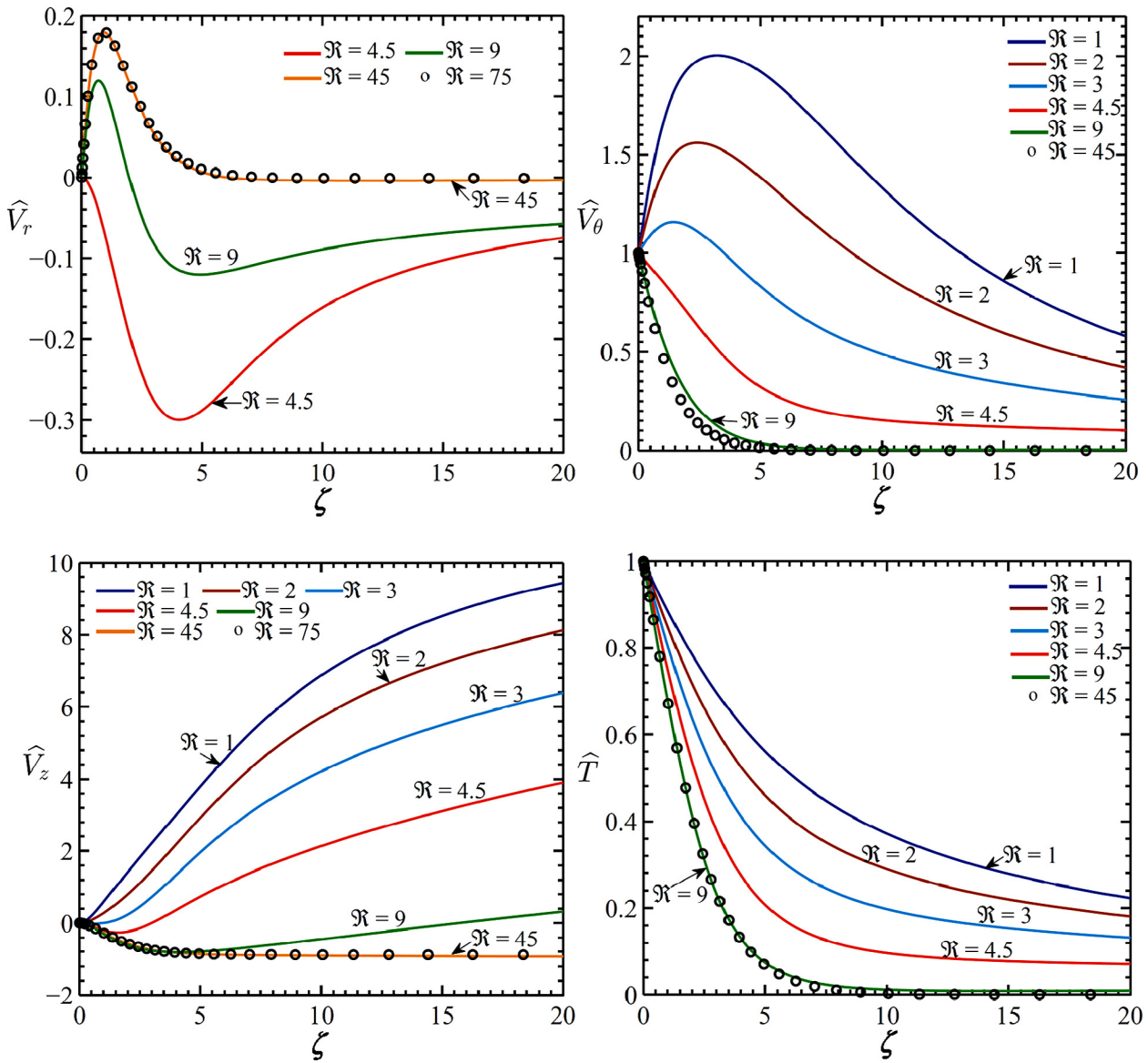


Fig. 8. (Colour online) ζ -distributions of various non-dimensional variables (\hat{V}_r , \hat{V}_θ , \hat{V}_z and \hat{T}) at various non-dimensional radius \mathfrak{R} . [CFD simulation is performed at $Gr_{mc} = 15$, $Pr = 0.7068$. Note that \hat{V}_θ and \hat{T} approach their respective self-similarity profiles early (see the profiles at $\mathfrak{R} = 9$). \hat{V}_r and \hat{V}_z approach their respective self-similarity profiles much later (see the profiles at $\mathfrak{R} = 45$).]

Nu versus \mathfrak{R} obtained from the similarity theory and Nu versus \mathfrak{R} obtained from a separate CFD simulation for $g = 0$. In both similarity theory and the simulation for $g = 0$, the effect of buoyancy is neglected; therefore, both similarity theory and the simulation for $g = 0$ represent forced convection. However, in the similarity theory, ordinary differential Eqs. (24)–(27) are solved; whereas in the CFD simulation, we achieve the solution of the set of partial differential Eqs. (1)–(5) with $g = 0$ by invoking the axisymmetric swirl model for the Navier-Stokes equations in Fluent and switching off the gravity term. The quantitative difference between Nu versus \mathfrak{R} obtained from the similarity theory and that obtained from the CFD simulation for $g = 0$ is displayed in Fig. 10a and b (for $10 \leq \mathfrak{R} \leq 20$). Unlike the similarity theory, the Nu versus \mathfrak{R} curve for forced convection obtained from the CFD simulations is not exactly linear. Furthermore, the prediction of similarity theory is always greater than the prediction of the CFD simulation for $g = 0$; the relative difference may be appreciable at small values of \mathfrak{R} . At sufficiently large \mathfrak{R} , the results of the similarity theory and the CFD results come closer.

Some general observations can be made from Fig. 10a while comparing the curves of Nu versus \mathfrak{R} for mixed convection (shown here for three representative Gr_{mc}) with the curves of Nu versus \mathfrak{R} for forced convection ($g = 0$). When \mathfrak{R} is small the value of Nu for mixed convection is less than the value of Nu for forced convection. However, with an increase in \mathfrak{R} , Nu for mixed convection overtakes Nu for forced convection. The point of crossover shifts to a greater \mathfrak{R} -value with a decrease in Gr_{mc} (see Fig. 10a).

The above mentioned features are illustrated below using three representative cases, viz. $g = 0$, $Gr_{mc} = 10$ and $Gr_{mc} = 25$. A schematic representing mixed convection ($Gr_{mc} \neq 0$) is shown in Fig. 11a. Fluid enters into the region R-1 through the locus of $\hat{V}_r = 0$ (due to nonzero \hat{V}_z). The radial outflow for the displayed portion of R-1 is also shown. At any non-dimensional radius \mathfrak{R} , the magnitude of radial outflow depends on the ζ -variation of \hat{V}_r . When \mathfrak{R} is sufficiently large, so that self-similarity is attained, the ζ -variation of \hat{V}_r will be independent of \mathfrak{R} (see Section 3.2). Consider such a large \mathfrak{R} for $Gr_{mc} = 25$. Suppose this large non-

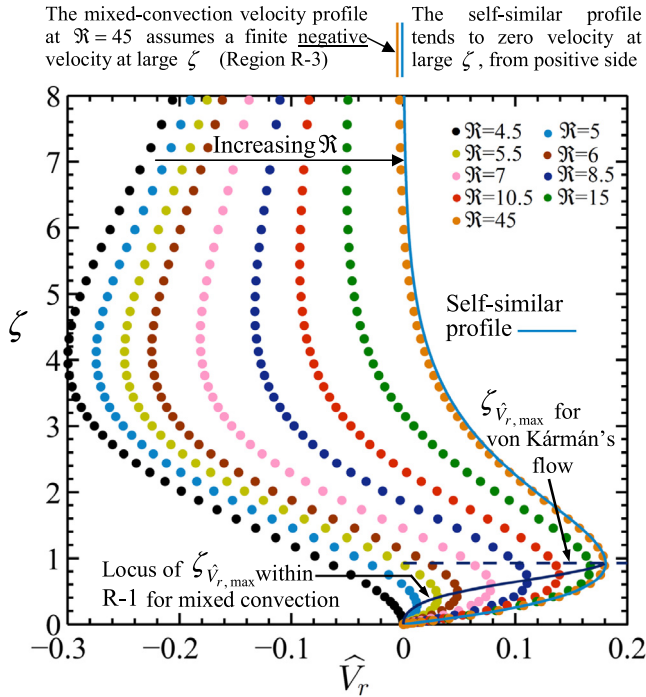


Fig. 9. (Colour online) Non-dimensional radial velocity (\hat{V}_r) profiles at various \mathfrak{R} for mixed convection and their progressive development with an increase in \mathfrak{R} towards the self-similar \hat{V}_r -profile for forced convection. [CFD simulation is performed at $Gr_{mc} = 15$, $Pr = 0.7068$. The lowest \mathfrak{R} shown in this diagram (i.e. $\mathfrak{R} = 4.5$) indicates the \mathfrak{R} -location from where the region R-1 just starts. The asymptotic values at large ζ for the velocity profiles at $\mathfrak{R} = 45$ are shown at the top of the diagram.].

dimensional radius is \mathfrak{R}_s . At \mathfrak{R}_s , the attainment of self-similarity is also expected for the cases of $g = 0$ and $Gr_{mc} = 10$. Thus, at \mathfrak{R}_s , ζ -profiles of \hat{V}_r within R-1 for $g = 0$, $Gr_{mc} = 10$ and $Gr_{mc} = 25$ will be identical. Consequently, at \mathfrak{R}_s , the non-dimensional radial outflow (\hat{Q}_r) for all these three cases will be the same. \hat{Q}_r is defined as:

$$\hat{Q}_r = Q_r / (\sqrt{v\Omega}\pi r^2) \tag{34}$$

where, the dimensional radial outflow Q_r equals $2\pi r \int_0^z V_r dz$. z^* is the location where a circumferential plane (on which r is constant) cuts the locus of $\hat{V}_r = 0$.

Now, consider that v and Ω are fixed; and, Gr_{mc} is varied by changing $(T_w - T_\infty)$. Under this situation, for all three cases (i.e. $g = 0$, $Gr_{mc} = 10$ and $Gr_{mc} = 25$), the values of r_s ($r_s \equiv \mathfrak{R}_s \sqrt{v/\Omega}$) will be same; furthermore, the values of $Q_{r,s}$ (Q_r at r_s) will be same. $Q_{r,s}$ is entrained within R-1 through the locus of $\hat{V}_r = 0$. The starting point of the locus of $\hat{V}_r = 0$ is indicated by O_f in Fig. 11a. By comparing Fig. 11c and d, it can be stated that the point O_f shifts to a greater radius with an increase in Gr_{mc} . Thus, for the same $Q_{r,s}$, the effective area for inflow within R-1 is decreased with an increase in Gr_{mc} . (For the case of $g = 0$, the point O_f occurs at disc-centre; therefore, the effective area for inflow is the highest). Smaller effective area (for a greater value of Gr_{mc}) results into a greater downward axial velocity V_z . This fact is demonstrated in Fig. 11b.

Cold fluid enters into R-1 through a downward axial flow; thus, heat is transferred from hot disc-surface to the fluid. A greater axial velocity causes a greater heat transfer. This is reflected in the distributions of temperature. The temperature-contours for $Gr_{mc} = 10$ and $Gr_{mc} = 25$ are shown in Fig. 11c and d, respectively. In order to compare the values of \hat{T} , in both Fig. 11c and d, three dotted lines are inserted at three representative ζ -

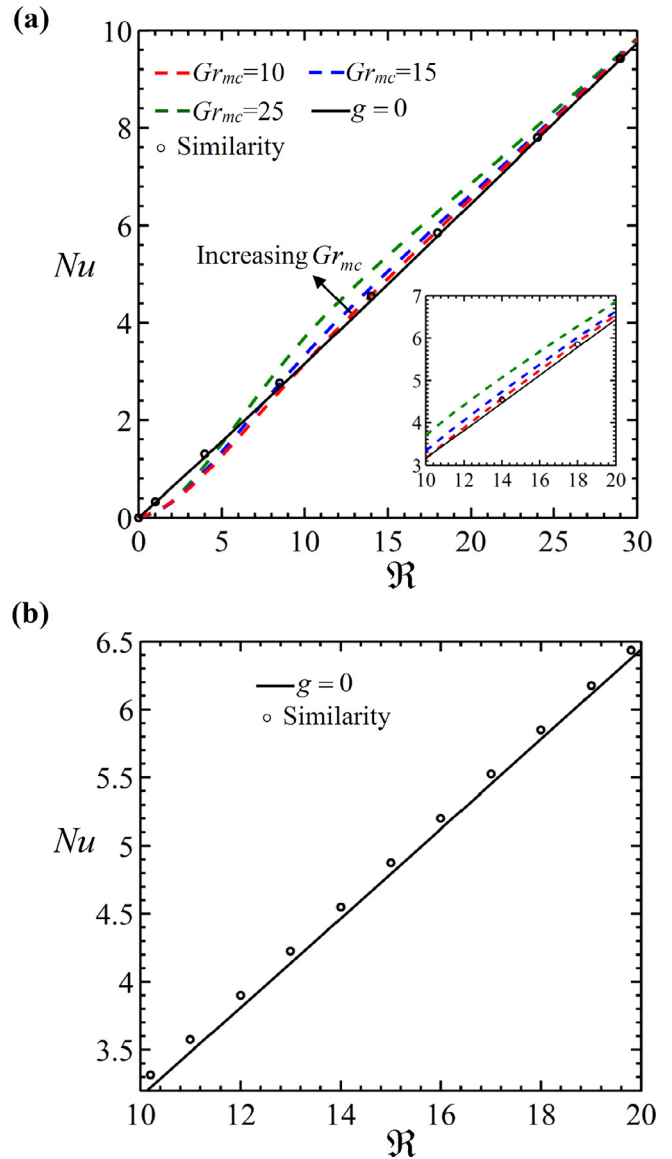


Fig. 10. (Colour online) Effect of increasing Gr_{mc} on the distribution of local Nusselt number (Nu). (a) CFD solutions for mixed convection at three different values of Gr_{mc} , CFD solution for forced convection ($g = 0$), and similarity solution for forced convection (b) Magnified comparison between similarity solution and CFD solution with $g = 0$. (All calculations correspond to $Pr = 0.7068$.)

locations are the same at which the radial variations of \hat{V}_z are shown in Fig. 11b. It is observed that within R-1, the temperature of fluid at any ζ is greater for the case of $Gr_{mc} = 10$ as compared to the case of $Gr_{mc} = 25$. The above description explains, for intermediate values of \mathfrak{R} , how Nu for mixed convection overtakes Nu for forced convection, and, why Nu increases with increasing Gr_{mc} .

The other interesting phenomenon occurs close to the disc-centre. It is discussed previously that within R-2, a plume is formed. Therefore, within R-2, $\partial T/\partial z$ is small. For $g = 0$, R-2 does not exist. Consequently, at small non-dimensional radius \mathfrak{R} , Nu for mixed convection is less than Nu for pure forced convection ($g = 0$). The starting point of the locus of $\hat{V}_z = 0$ is indicated by O_m in Fig. 11a. By comparing Fig. 11c and d, it can be stated that the point O_m shifts to a greater radius with an increase in Gr_{mc} . However, the radial shift of O_m is less as compared to O_f , therefore, the distance between O_m and O_f increases with an increase in Gr_{mc} . For this reason, the \mathfrak{R} -distribution of the Nu is affected more due to the radial shift of O_f as compared to the radial shift of O_m . Fig. 10a

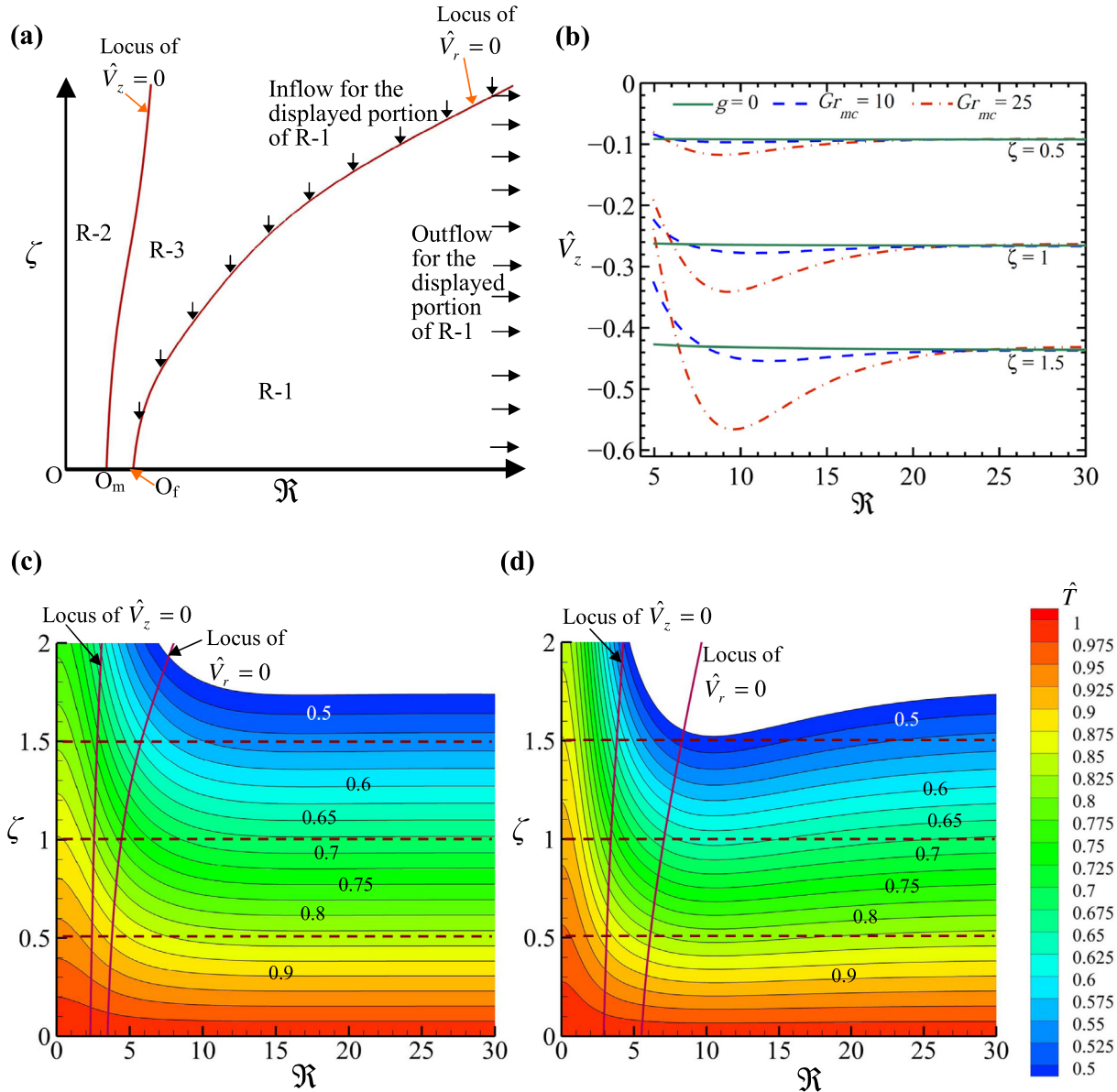


Fig. 11. (Colour online) Depiction of the physical processes close to the solid surface for interpreting why buoyancy increases the value of Nu (over the case of pure forced convection) within the region R-1 and how the effect increases with increasing Gr_{mc} . (a) a schematic exhibiting three fluid dynamic regions (R-1, R-2 and R-3), three important points O, O_m and O_f , and, the directions of inflow and outflow for the displayed portion of R-1; (b) effect of increasing Gr_{mc} on the \mathfrak{R} -distributions of \hat{V}_z (calculations shown at three representative ζ close to the solid surface); (c) contours of \hat{T} for $Gr_{mc} = 10$; (d) contours of \hat{T} for $Gr_{mc} = 25$.

shows that when Gr_{mc} increases from 10 to 25, the value of Nu at small \mathfrak{R} ($\mathfrak{R} < 5$) alters insignificantly, and the point of crossover (between the curve for forced convection and a curve for mixed convection) arrives at a smaller \mathfrak{R} -value.

3.4. Comments on $C_{m,r}$ and \overline{Nu}

$C_{m,r}$ and \overline{Nu} are two important output parameters which are defined in Section 2.2 (Eqs. (20) and (22), respectively). The averaged thermo-fluid-dynamic behaviour of a disc segment, extending from disc-centre up to a radius r , can be assessed from the values of \overline{Nu} and $C_{m,r}$. Table 2 shows the calculated values of \overline{Nu} and $C_{m,r}$ obtained from CFD simulations for four representative values of Gr_{mc} (5, 10, 15 and 25), from a CFD simulation for $g = 0$, and, from the similarity theory. Both similarity solution and the CFD solution for $g = 0$ represent forced convection, whereas the CFD solutions for the four Gr_{mc} represent various mixed convective con-

ditions. For all these cases, \overline{Nu} and $C_{m,r}$ are calculated at five representative \mathfrak{R} -locations (5, 10, 20, 50 and 100).

Table 2 shows that when \mathfrak{R} is large (e.g. $\mathfrak{R} = 100$) both \overline{Nu} and $C_{m,r}$ for mixed convection are close to their respective forced convective values. With a decrease in \mathfrak{R} , the difference between $C_{m,r}$ for mixed convection and $C_{m,r}$ for forced convection increases. The difference is significant for small \mathfrak{R} (see the case of $\mathfrak{R} = 5$). When \mathfrak{R} is small (e.g. $\mathfrak{R} = 5$) and Gr_{mc} is large (e.g. $Gr_{mc} = 25$), $C_{m,r}$ for mixed convection is negative, whereas $C_{m,r}$ for forced convection is positive. The negative value of $C_{m,r}$ occurs because at small \mathfrak{R} , $(\partial \hat{V}_\theta / \partial \zeta)_{\zeta=0}$ is positive (Fig. 8). The sign convention for $C_{m,r}$ is adopted from reference [35]. The positive $C_{m,r}$ signifies that power has to be supplied from external source to maintain a steady rotational speed Ω . Conversely, the negative $C_{m,r}$ implies that, in mixed convection, the fluid, instead of absorbing, may rather supply power to a small segment of the disc! (Overall, the disc needs power supply from an external source.)

Table 2
 \overline{Nu} and $C_{m,r}$ at various non-dimensional radius \mathfrak{R} for four representative values of Gr_{mc} (All calculations correspond to $Pr = 0.7068$).

\mathfrak{R}	Gr_{mc}	\overline{Nu} for mixed convection from CFD	\overline{Nu} for $g = 0$ from CFD	\overline{Nu} for forced convection from similarity	$C_{m,r}$ for mixed convection from CFD	$C_{m,r}$ for $g = 0$ from CFD	$C_{m,r}$ for forced convection from similarity
5	5	1.118	1.542	1.625	0.278	0.389	0.387
	10	1.020			0.122		
	15	1.053			0.020		
	25	1.167			−0.099		
10	5	2.650	3.120	3.250	0.169	0.194	0.193
	10	2.719			0.151		
	15	2.872			0.143		
	25	3.216			0.141		
20	5	6.046	6.354	6.500	0.091	0.095	0.097
	10	6.244			0.091		
	15	6.464			0.091		
	25	6.952			0.094		
50	5	16.085	16.183	16.250	0.039	0.039	0.039
	10	16.220			0.039		
	15	16.320			0.039		
	25	16.516			0.039		
100	5	32.463	32.472	32.500	0.019	0.019	0.019
	10	32.534			0.019		
	15	32.581			0.019		
	25	32.641			0.019		

A few interesting observations derived from Table 2 about the trend of \overline{Nu} are given below. At a small \mathfrak{R} , when Gr_{mc} increases from 5 to 25, no substantial difference is found in the values of \overline{Nu} . At an intermediate \mathfrak{R} , when Gr_{mc} increases from 5 to 25, \overline{Nu} increases. At a large \mathfrak{R} , \overline{Nu} becomes nearly invariant with a change in Gr_{mc} . Necessary explanations supporting these observations are already provided in Section 3.3.

In this connection, the question, whether the heat transfer due to rotation is opposed by the heat transfer due to buoyancy, can be addressed. Fig. 10 and Table 2 show that the answer is not straightforward. For small values of \mathfrak{R} , buoyancy opposes the effect of rotation. Thus, Nu for mixed convection is less than Nu for forced convection (Fig. 10a). Same qualitative trend is present in the variation of \overline{Nu} (Table 2). However, at an intermediate \mathfrak{R} , when Gr_{mc} is sufficiently large, \overline{Nu} for mixed convection may exceed \overline{Nu} for forced convection. It is so because at an intermediate \mathfrak{R} , Nu for mixed convection is greater than Nu for forced convection, and Nu increases with an increase in Gr_{mc} (Fig. 10a). In other words, at an intermediate \mathfrak{R} , buoyancy facilitates the effect of rotation. At large \mathfrak{R} , the effect of buoyancy is insignificant, and, heat transfer is mainly governed by the effect of rotation.

4. Conclusion

The paper presents a comprehensive and systematic, theoretical and computational study of mixed convection above a heated rotating disc. The fluid flow field is much more complex here as compared to von Kármán's original solution (which took into account only the effect of disc rotation), since the effects of buoyancy and rotation are simultaneously present and they interact non-linearly in a complex manner. The self-similarity of von Kármán's flow field is lost, and the present paper establishes, for the first time, that the flow field above a heated rotating disc is divided into three distinct fluid dynamic regions. In region 1 (R-1), \hat{V}_r is positive and \hat{V}_z is negative (such directions of the velocity components are characteristic of von Kármán's flow or pure forced convection). In region 2 (R-2), \hat{V}_r is negative and \hat{V}_z is positive (such directions of the velocity components are characteristic of pure natural convection near a static disc surface). In region 3

(R-3), both \hat{V}_r and \hat{V}_z are negative. The three regions are demarcated by the loci of $\hat{V}_z = 0$ and $\hat{V}_r = 0$.

The characteristics of the original von Kármán's flow are retained within the region R-1; however, the quantitative details are different at intermediate values of non-dimensional radius \mathfrak{R} due to the presence of buoyancy. For fixed values of Gr_{mc} (Grashof number for mixed convection, Eq. (12)) and Pr (Prandtl number), when \mathfrak{R} is sufficiently large, the contour lines shown in Figs. 4–7 are nearly parallel, and, the ζ -distributions of \hat{V}_r , \hat{V}_θ , \hat{V}_z and \hat{T} within the region R-1 are almost independent of \mathfrak{R} (see Fig. 8). These two observations indicate that, in region R-1, the CFD solutions corresponding to mixed convection approach the self-similar solutions corresponding to forced convection. Fig. 8 shows that for fixed Gr_{mc} and Pr , \hat{V}_θ and \hat{T} approach their respective self-similarity profiles early (see the profiles at $\mathfrak{R} = 9$); and, \hat{V}_r and \hat{V}_z approach their respective self-similarity profiles much later (see the profiles at $\mathfrak{R} = 45$). When self-similarity is attained the value of $\hat{\delta}_r$ (8.14) is greater than the value of $\hat{\delta}$ (5.5). It is to be realised that even though the forced convection results are obtained asymptotically at large \mathfrak{R} within the region R-1 showing the dominance of forced convection mechanism, the fluid retains the signature of natural convection even at large values of \mathfrak{R} in the region R-3 where there is an inward radial velocity.

Within the region R-2, a plume is formed which is symptomatic of the dominance of natural convective mechanism. The plume is fed by a radially inward flow, and it drives the fluid axially upward. The bending of streamlines within R-2 (Fig. 4) signifies a conversion of radial velocity into axial velocity. The magnitude of the upward axial velocity in the plume is significantly greater than the downward entrainment velocity at the upper edge of the computational domain (Fig. 5). Unlike a plume that develops above a heated static disc, the \hat{V}_θ component for a plume developed above a rotating disc is non-zero, so the hot fluid rises with a swirling motion. Thus, even in the central portion of the disc where the solution is dominated by the effects of buoyancy, the fluid retains a signature of the disc rotation.

A limiting case, in which the effect of buoyancy is absent, is devised here by setting $g = 0$ in the CFD simulations. This limiting case represents forced convection for which a similarity theory is

also presented. Ordinary differential Eqs. (24)–(27) are solved for the similarity theory; whereas in CFD simulation, partial differential Eqs. (1)–(5), by imposing $g = 0$, are solved. Although both methods show the same trend, the present paper shows that there are quantitative differences between the results of CFD simulations for forced convection and the similarity theory (see Fig. 10a and b). Unlike the similarity theory, the Nu versus \mathfrak{R} curve for forced convection obtained from the CFD simulations is not exactly linear. Furthermore, the prediction of similarity theory is always greater than the prediction of the CFD simulation for $g = 0$; the relative difference may be appreciable at small values of \mathfrak{R} . At sufficiently large \mathfrak{R} , the results of the similarity theory approach the CFD results.

The complex non-linear interactions between the effects of rotation and buoyancy are quantitatively presented in the many Figures and Tables of this paper. We conclude here by highlighting three rather strange, non-intuitive outcomes of this non-linear interaction. The first strange feature is unearthed in Fig. 6b of the present investigation, which shows that within a portion of regions R-2 and R-3, \hat{V}_θ of the fluid can be significantly greater than unity. This signifies that there are fluid particles which rotate with swirl velocity much greater than the tangential velocity of the disc at the same radius. In the region where \hat{V}_θ exceeds 1, the ζ -distribution of \hat{V}_θ is very different from that obtained in von Kármán's flow (see Fig. 8). Within this region, $(\partial\hat{V}_\theta/\partial\zeta)_{\zeta=0}$ is positive, whereas for von Kármán's flow, $(\partial\hat{V}_\theta/\partial\zeta)_{\zeta=0}$ is negative. The consequence of this unusual ζ -distribution of \hat{V}_θ is reflected in the results of non-dimensional moment coefficient ($C_{m,r}$) given in Table 2. For large Gr_{mc} and small \mathfrak{R} (e.g., see the case $Gr_{mc} = 25$ and $\mathfrak{R} = 5$ in Table 2), $C_{m,r}$ is found to be negative. For von Kármán's flow, $C_{m,r}$ is positive, and, the positive value implies that power has to be supplied from external source to maintain a steady rotational speed Ω . Conversely, the negative $C_{m,r}$ implies that, in mixed convection, the fluid, instead of absorbing, may rather supply power to a small segment of the disc! (Overall, the disc needs power supply from an external source.)

The second strange feature is displayed in Fig. 4 where it is discovered that there is a sensitive spot on the upper boundary of the computational domain such that two streamlines originating at two neighbouring points may end up in very different final portions of the trajectories, one being drawn into the forced convection domain (moving nearly parallel to the disc surface) while the other is ejected through the plume (moving nearly vertically upward).

The third strange outcome of the non-linear interaction of rotation and buoyancy is in the value of the resultant Nusselt number. It is found that although in terms of the direction of radial motion the effect of buoyancy counteracts the effect of rotation (disc-rotation pushes the fluid radially outward, whereas buoyancy tends to create a radially inward flow), the effects of the mutual interaction between buoyancy and rotation on the heat transfer rate is complex. This can be appreciated from the Nu versus \mathfrak{R} curves shown in Fig. 10a. If ΔNu represents the difference between the Nusselt number for mixed convection and that for pure forced convection (i.e. $\Delta Nu = Nu_{mixed} - Nu_{forced}$), then the present results

establish that not only ΔNu depends non-linearly on the value of Gr_{mc} but the sign of ΔNu also does change. For small values of \mathfrak{R} , $Nu_{mixed} < Nu_{forced}$. It is so because at small \mathfrak{R} , a plume is formed, consequently, $(\partial\hat{T}/\partial\zeta)_{\zeta=0}$ is small (Figs. 7 and 8). For intermediate values of \mathfrak{R} , $Nu_{mixed} > Nu_{forced}$, and ΔNu increases with increasing Gr_{mc} . This occurs because of the increase in \hat{V}_z near the solid surface with increasing Gr_{mc} (Fig. 11). For large \mathfrak{R} , $Nu_{mixed} \rightarrow Nu_{forced}$ from above. Thus, one may conclude that, in terms of heat transfer mechanisms, buoyancy opposes the effect of rotation at small \mathfrak{R} , whereas buoyancy facilitates the effect of rotation at intermediate \mathfrak{R} ; and, at large \mathfrak{R} , the effect of buoyancy is negligible, and, heat transfer is chiefly controlled by the effect of rotation.

Appendix A. Choice of grids near the axis of rotation and further computations showing the suitability of axis boundary condition

A.1. Fine details of grid independence test near the axis of rotation

In Section 2.4, it is mentioned that both velocity and temperature fields change rapidly at small \mathfrak{R} and slowly at large \mathfrak{R} . Therefore, apart from applying non-uniform grid distribution in the z -direction, we have used non-uniform grid distribution also in the r -direction. As a result, it has been possible to accommodate a large number of grid points close to the axis of rotation. The first grid attached to the axis of rotation is the smallest, and the grid-size increases progressively with an increase in radius. When \mathfrak{R} is sufficiently large (that the spatial variations of temperature and velocity fields are no longer drastic) uniform grid distribution is used in the r -direction. For the computations reported in this paper, we have used non-uniform grid spacing for $\mathfrak{R} \leq 50$, and uniform grid spacing for $\mathfrak{R} > 50$.

An overall grid independence study is given in Section 2.4. Here, we focus our attention very close to the axis of rotation ($0 \leq \mathfrak{R} \leq 5$) to assess how well our CFD results are able to capture the physics in a region of the highest gradients of the flow variables. Table A.1 displays the number of grids in the r direction within $0 \leq \mathfrak{R} \leq 5$. It may be noted that we have used 71 grid points in this small region of flow field in the standard grid used for all CFD results shown in Figs. 3–11 and Table 2. Table A.1 and Fig. A.1 together show that when the number of grids (in the r direction) within $0 \leq \mathfrak{R} \leq 5$ is almost doubled (i.e. from 71 for standard-grid-distribution to 136 for fine-grid-distribution), the CFD results vary negligibly. Table A.1 and Fig. A.1 are two representative tests out of several tests which have been carried out to verify the near-axis details. The positive outcome of such investigations gives us confidence in the accuracy of the results reported in this paper.

A.2. 'Axis boundary condition' of Fluent

In the literature, differences between axisymmetric and full 3-D simulations have been reported [40]. We implemented the 'axis boundary condition' to reduce computational time since a large number of separate simulations were needed for the present study

Table A.1
Grid independence test (CFD data for $Gr_{mc} = 15$, $Pr = 0.7068$).

Size of the CFD domain	Grid distribution	Number of grids in r and z directions	Total number of computational cells	Number of grids in the r direction within $0 \leq \mathfrak{R} \leq 5$	Nu at $\mathfrak{R} = 5$ from CFD simulations	\bar{Nu} over $0 \leq \mathfrak{R} \leq 5$ from CFD simulations
$[\mathfrak{R}, \zeta] = [0, 0]$ to $[\mathfrak{R}, \zeta] = [215, 60]$	Coarse	(235 × 129)	30315	18	1.32	1.04
	Standard	(413 × 197)	81361	71	1.33	1.05
	Fine	(523 × 264)	138072	136	1.33	1.05

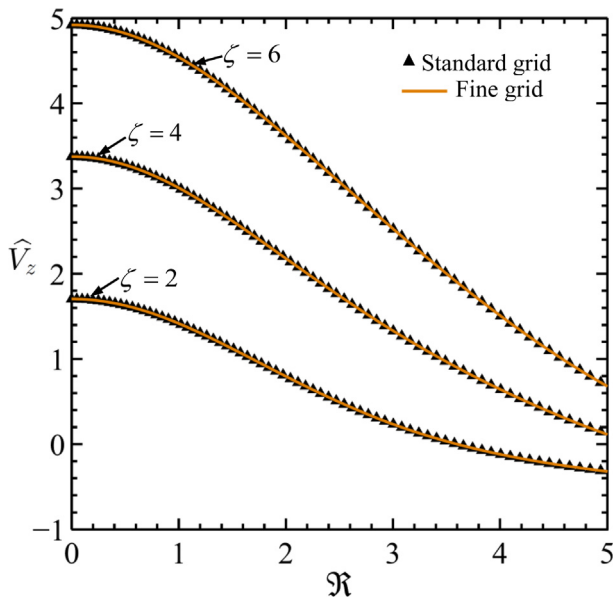


Fig. A.1. (Colour online) Fine details of the grid independence test close to the axis of rotation. (CFD simulations are performed at $Gr_{mc} = 15$, $Pr = 0.7068$. 71 grid points are used in the standard grid within the small region $0 \leq \mathfrak{R} \leq 5$. Results are shown for three different heights (ζ) above the disc.)

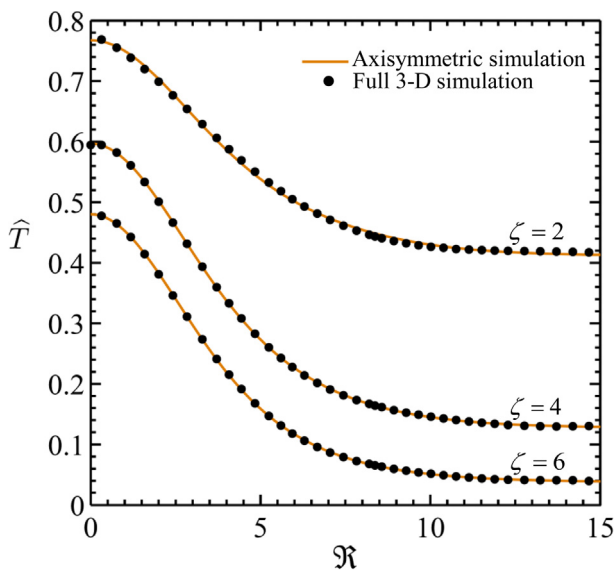


Fig. A.2. (Colour online) The prediction of axisymmetric CFD simulation versus the result of full three dimensional CFD simulation. (CFD simulations are performed at $Gr_{mc} = 10$, $Pr = 0.7068$. Results are shown for three different heights (ζ) above the disc.)

and an axisymmetric flow field was expected. In order to determine whether this boundary condition can produce accurate solutions, particularly very close to the axis of rotation, full three-dimensional computations were also undertaken. These further computations showed that there is no discernible difference between the solutions of these carefully conducted full 3-D solutions and those reported in this paper. Fig. A.2 establishes the equivalence of the two solutions.

References

- [1] T. von Kármán, Über laminare und turbulente Reibung, *Z. Angew. Math. Mech.* 1 (1921) 233–252.
- [2] A. Guha, S. Sengupta, Analysis of von Kármán's swirling flow on a rotating disc in Bingham fluids, *Phys. Fluids* 28 (1) (2016) 013601–1–013601–30.
- [3] P.J. Zandbergen, D. Dijkstra, Von Kármán swirling flows, *Annu. Rev. Fluid Mech.* 19 (1) (1987) 465–491.
- [4] R.J. Lingwood, Absolute instability of the Ekman layer and related rotating flows, *J. Fluid Mech.* 331 (1997) 405–428.
- [5] C. Davies, P.W. Carpenter, Global behaviour corresponding to the absolute instability of the rotating-disc boundary layer, *J. Fluid Mech.* 486 (2003) 287–329.
- [6] M. Turkyilmazoglu, Purely analytic solutions of the compressible boundary layer flow due to a porous rotating disk with heat transfer, *Phys. Fluids* 21 (10) (2009) 106104.
- [7] C. Thomas, C. Davies, Global stability of the rotating-disc boundary layer with an axial magnetic field, *J. Fluid Mech.* 724 (2013) 510–526.
- [8] Y. Burnishev, V. Steinberg, Torque and pressure fluctuations in turbulent von Karman swirling flow between two counter-rotating disks I, *Phys. Fluids* 26 (5) (2014) 055102.
- [9] A.J. Cooper, J.H. Harris, S.J. Garrett, M. Özkan, P.J. Thomas, The effect of anisotropic and isotropic roughness on the convective stability of the rotating disk boundary layer, *Phys. Fluids* 27 (1) (2015) 014107.
- [10] S.J. Garrett, A.J. Cooper, J.H. Harris, M. Özkan, A. Segalini, P.J. Thomas, On the stability of von Kármán rotating-disc boundary layers with radial anisotropic surface roughness, *Phys. Fluids* 28 (1) (2016) 014104.
- [11] V.W. Ekman, On the influence of the earth's rotation on ocean currents, *Ark. Mat. Astron. Fys.* 2 (11) (1905) 1–53.
- [12] G.K. Batchelor, Note on a class of solutions of the Navier-Stokes equations representing steady rotationally-symmetric flow, *Q. J. Mech. Appl. Math.* 4 (1951) 29–41.
- [13] K. Stewartson, On the flow between two rotating coaxial disks, *Proc. Camb. Philos. Soc.* 49 (1953) 333–341.
- [14] A. Guha, S. Sengupta, The fluid dynamics of the rotating flow in a Tesla disc turbine, *Eur. J. Mech.-B/Fluids* 37 (2013) 112–123.
- [15] L.A. Dorfman, Heat and mass transfer near rotating surfaces, *J. Eng. Phys. Thermophys.* 22 (2) (1972) 247–257.
- [16] F. Kreith, *Convection heat transfer in rotating systems*, Adv. Heat Trans., vol. 5, Academic Press, New York, 1968, pp. 129–251.
- [17] J.M. Owen, R.H. Rogers, *Flow and Heat Transfer in Rotating Disc Systems, Rotor-Stator Systems*, vol. 1, Research Studies Press, Taunton, UK, 1989.
- [18] I.V. Shevchuk, *Convective Heat and Mass Transfer in Rotating Disk Systems*, Springer Verlag, Berlin, Heidelberg, 2009.
- [19] E.C. Cobb, O.A. Saunders, Heat transfer from a rotating disk, *Proc. R. Soc. London A: Math. Phys. and Eng. Sci.* 236 (1206) (1956) 343–351.
- [20] C.J. Elkins, J.K. Eaton, Heat transfer in the rotating disk boundary layer. Stanford University, Department of Mechanical Engineering, Thermosciences Division Report TSD-103. Stanford University (USA), 1997.
- [21] B.E. Launder, B.I. Sharma, Application of the energy-dissipation model of turbulence to the calculation of flow near a spinning disc, *Lett. Heat Mass Trans.* 1 (2) (1974) 131–137.
- [22] R.J. Lingwood, An experimental study of absolute instability of the rotating-disk boundary-layer flow, *J. Fluid Mech.* 314 (1996) 373–405.
- [23] C. Wagner, Heat transfer from a rotating disk to ambient air, *J. Appl. Phys.* 19 (9) (1948) 837–839.
- [24] M. Zakerullah, J.A.D. Ackroyd, Laminar natural convection boundary layers on horizontal circular discs, *Zeitschrift für Angewandte Mathematik und Physik ZAMP* 30 (3) (1979) 427–435.
- [25] J.H. Merkin, Free convection above a heated horizontal circular disk, *Zeitschrift für Angewandte Mathematik und Physik ZAMP* 34 (5) (1983) 596–608.
- [26] R.J. Whittaker, J.R. Lister, Steady axisymmetric creeping plumes above a planar boundary. Part 2. A distributed source, *J. Fluid Mech.* 567 (2006) 379–397.
- [27] A. Guha, K. Pradhan, A unified integral theory of laminar natural convection over surfaces at arbitrary inclination from horizontal to vertical, *Int. J. Therm. Sci.* 111 (2017) 475–490.
- [28] A. Guha, S. Sengupta, Effects of finiteness on the thermo-fluid-dynamics of natural convection above horizontal plates, *Phys. Fluids* 28 (6) (2016) 063603–1–063603–29.
- [29] A. Guha, S. Samanta, Closed-form analytical solutions for laminar natural convection on horizontal plates, *ASME J. Heat Trans.* 135 (10) (2013) 102501–1–102501–9.
- [30] O. Shishkina, S. Grossmann, D. Lohse, Heat and momentum transport scalings in horizontal natural convection, *Geophys. Res. Lett.* 43 (2016) 1219–1225.
- [31] J. Arrieta-Sanagustín, M.G. Blyth, Mixed convection above a rotating disk, *Quart. J. Mech. Appl. Math.* 66 (3) (2013) 317–331.
- [32] B. Gebhart, Effect of viscous dissipation in natural convection, *J. Fluid Mech.* 14 (2) (1962) 225–232.
- [33] H. Schlichting, K. Gersten, *Boundary-Layer Theory*, 8th edition., Springer, New Delhi, India, 2004.
- [34] L.C. Burmeister, *Convective Heat Transfer*, John Wiley & Sons, New York, USA, 1983.
- [35] P.R.N. Childs, *Rotating Flow*, Butterworth-Heinemann Press, Oxford, UK, 2011.
- [36] *Fluent 6.3 User's Guide*, Fluent Inc., Central Source Park, 10 Cavendish Court, Lebanon, NH 03766, USA, 2006.
- [37] A. Guha, J.B. Young, Time-marching prediction of unsteady condensation phenomena due to supercritical heat addition, in: *Turbomachinery: Latest Developments in a Changing Scene*, IMechE, London, 1991, ISBN 0852987617, pp. 167–177.

- [38] Y. Mei, A. Guha, Implicit numerical simulation of transonic flow through turbine cascades on unstructured grids, *Proc. Inst. Mech. Eng, Part A: J. Power Energy* 219 (1) (2005) 35–47.
- [39] B. Bradie, *A Friendly Introduction to Numerical Analysis*, Pearson Education, New Delhi, India, 2007.
- [40] R.F. Susan-Resiga, S. Muntean, C. Tanasa, A. Bosioc, Three-dimensional versus two-dimensional axisymmetric analysis for decelerated swirling flows. In: *Proceedings of the 13th International Conference on Fluid Flow*, Budapest, Hungary, 2009.